

Article

# Highly Integrated Wideband Transmit/Receive Module for X-Band SAR Applications

Francesco de Paulis <sup>1,\*</sup>, Daniele Di Giuliomaria <sup>2</sup>, Antonio Fina <sup>3</sup>, Marco Amici <sup>2</sup>, Giovanni Mannocchi <sup>2</sup>, Alessandro Di Carlofelice <sup>1</sup>, Andrea Fiaschetti <sup>2</sup>, Piero Tognolatti <sup>1</sup> and Antonio Orlandi <sup>1</sup>

<sup>1</sup> Department of Industrial and Information Engineering and Economics, University of L'Aquila, Via G. Gronchi 18, Loc. Pile, 67100 L'Aquila, Italy

<sup>2</sup> Thales Alenia Space Italia, Via Saccomuro, 00131 Rome, Italy

<sup>3</sup> Thales Alenia Space Italia, Via Giandomenico Cassini 6, Loc. Pile, 67100 L'Aquila, Italy

\* Correspondence: francesco.depaulis@univaq.it

**Abstract:** The roadmaps of satellite-based synthetic aperture radar (SAR) systems show a trend that requires a continuous improvement of the active antenna in terms of operating bandwidth, scanning angle capability, and swath width, thus leading to the demand for increased RF power and better power efficiency of the RF transmitter. Moreover, compact size and light weight are relevant objectives for making the overall SAR instrument appealing for future applications. The transmit/receive module (TRM) shown in this paper was developed while combining all these requirements in a cost-effective approach. A careful design of all relevant RF interconnects and passive devices was performed to ensure the largest output power from the last high-power amplifier of the transmitting chain, the lowest noise figure at the input of the receiving chain, and the calibration capability for appropriately tuning the TX and RX signal. The TRM was manufactured and experimentally tested to verify its performances. The measurement results show the superior performances of the proposed compact high-power large-bandwidth TRM. The achieved target objectives make the design of the proposed TRM readily applicable for the development of a compact, high-power, and highly integrated AESAs to be used for next-generation satellite constellations for Earth observation.

**Keywords:** satellites; earth observation; active electronic steerable antennas (AESAs); synthetic aperture radar (SAR); transmit/receive modules (TRM); wideband



**Citation:** de Paulis, F.; Di Giuliomaria, D.; Fina, A.; Amici, M.; Mannocchi, G.; Di Carlofelice, A.; Fiaschetti, A.; Tognolatti, P.; Orlandi, A. Highly Integrated Wideband Transmit/Receive Module for X-Band SAR Applications. *Appl. Sci.* **2023**, *13*, 801. <https://doi.org/10.3390/app13020801>

Academic Editor: Gang Lei

Received: 30 September 2022

Revised: 30 December 2022

Accepted: 31 December 2022

Published: 6 January 2023



**Copyright:** © 2023 by the authors. Licensee MDPI, Basel, Switzerland. This article is an open access article distributed under the terms and conditions of the Creative Commons Attribution (CC BY) license (<https://creativecommons.org/licenses/by/4.0/>).

## 1. Introduction

The current trends in the development of Earth observation systems are driven by a variety of applications involving many scientific research fields [1,2] such as weather forecast, monitoring of the Earth's surface (i.e., water and air pollution, thickness of the polar ice, etc.), agricultural purposes, geology, urban mapping, defense, and cartography, just to mention a few of them [3–10]. This trend leads to extremely challenging requirements for achieving better image resolution, finer feature discrimination, and higher penetration depth beyond ground and water surfaces; thus, more powerful instruments are required for appropriately equipping the constellation satellites [11]. This, in turn, translates into larger transmitting power, wider bandwidth, higher sensitivity, and wider steering capability of active electronic steerable antennas (AESAs) in synthetic aperture radar (SAR) systems [12–15].

A key element of this type of antenna system is the transmit/receive module (TRM) [16–19] that provides the appropriate amplitude and phase to the specific radiating element of the antenna array while it is transmitting and detects and amplifies the received signal while working in receiving mode [20,21]. The TRM developed and proposed in this paper has the capability to cover the whole X-band (8–12 GHz) associated with a very high transmitted power (>20 W): this enables very-high-resolution SAR. Its quad multilayer integration

and very compact design enables high steering angles, whereas the inclusion of delay lines allows for the avoidance of squinting when scanning the whole bandwidth. Several technological challenges are embedded into the design of the proposed TRM in terms of electrical performance, due to the very wide operational bandwidth radiated power, reduced size, and thermal requirements, in order to ensure proper module functionalities while working in different thermal (high temperature variability while the satellite is facing the sun) conditions and while being affected by harsh environments characterized by mechanical stress (vibrations) [22,23]. Although the promising compact solution proposed in [24–27] based on a challenging 3D packaging technology is able to successfully fulfill the electrical requirements, the thermal handling capabilities requires a more advanced and effective design in order to extract and dissipate the thermal energy from the large TRM array when they are actively driving the entire AESA.

The requirements for space technologies are very strict compared to commercial products in terms of mechanical stress, drift in the long-term performances of active devices due to the harsh environment, and lack of possibility for maintenance and electrical tuning of the module; thus, eventually, effective electrical and mechanical reliability are needed. Some of such space-compliant requirements are usually based on the European Space Agency (ESA) and military standard (MIL-STD) guidelines. Therefore, the materials and the manufacturing technologies used for building up the mechanical parts and electrical circuits can be selected on a quite limited set and they should be space-qualified in order to be able to deal with wide temperature variations, vibrations and mechanical shocks, to ensure immunity to space radiation and hermeticity in order to avoid any multipactor and corona effects. To meet these requirements, and to overcome the bandwidth and steering capabilities of the currently flying SAR solutions [28–30], a complete rework is proposed for the TRM.

The TRM design is based on a custom integrated core-chip based on SiGe technology and a custom integrated single-chip front-end (SCFE) in GaN technology [31] that were developed in the framework of the project ATOS [32]. Additionally, a new packaging approach based on a multi-module (quad-pack assembly) employing a new multilayer substrate [33], as well as an integral substrate package (ISP) approach, is proposed; moreover, the quad-pack layout makes the TRM package design suitable for integration on both direct reflect array (DRA) and reflector-type SAR antennas, thus achieving a higher antenna product design flexibility. The proposed innovative solution offers superior RF performances, with the output RF power increased by a factor of two and the bandwidth increased by a factor of three compared to the instrument on board the current flying satellite constellation [28,29]. Moreover, a reduced footprint, reduced part counts and electrical interfaces allow a more compact solution, helping the heat handling capabilities and a providing a reduced weight system, also enabling a denser packing of radiating elements for improved beam scanning performance, especially in the DRA antenna configuration. The overall performances of the proposed TRM were obtained by following a careful design of the package layout by adopting new solutions and their subsequent optimization for all microwave transitions within the full band of interest.

## 2. TRM Architecture

The block diagram in Figure 1 illustrates the architecture of each transmit/receive chain of the single TRM within the combined quad-module assembly.

The following main functional blocks may be distinguished:

- Control;
- Receiver;
- Transmit;
- Calibration.

The control block is composed of an integrated core-chip. Its main functions are to compensate the module-to-module amplitude and delay dispersion, to compensate the module amplitude and delay variation over temperature, to allow antenna beam shaping

by selecting the appropriate insertion amplitude and delay, and to route the RF signal through the appropriate path depending on the selected operative mode.

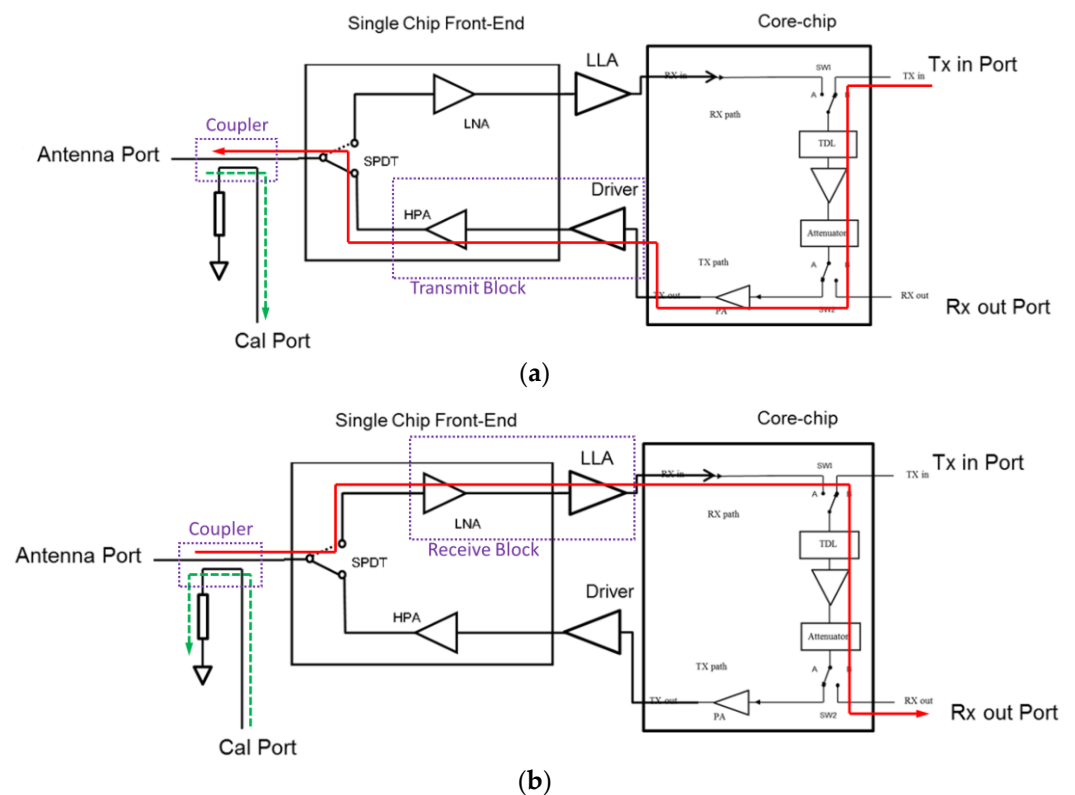


**Figure 1.** Identification of the paths of the electrical signals for the (a) TX mode of operation and (b) RX mode of operation. The corresponding calibration modes of operation involve also the directional coupler and the calibration port (Cal Port).

The receiver block is composed of the receive section of an integrated single-chip front-end (SCFE) and a low-level amplifier (LLA). This block has the function to amplify the signal received from the radiating element, while adding a low noise to it and keeping its linearity.

The transmitter block is composed of the transmit section of an integrated SCFE and a driver amplifier. This block has the function to amplify the signal to be delivered to the radiating element and be transmitted by it.

The calibration block is composed of a directional coupler.

The core-chip includes the phase shifting capability implemented using a true delay line (TDL) that is able to add the required time delay or phase shift, with minimum values of 1.56 ps corresponding to  $5.625^\circ$  at the center frequency (10 GHz). The delay (phase shift) can range from 0 to 100 ps, thus from 0 to  $360^\circ$  based on a 6-bit command for switching on and off the appropriate amplifier stages placed on each TDL section.

The two main modes of operation are the transmit and receives modes highlighted in Figure 1a,b, respectively, by the solid red lines. However, for the purpose of module calibration, both paths need to be evaluated and appropriately adjusted by varying the signal amplitude and phase; therefore, the corresponding calibration modes should be applied. This is done by defining the transmit calibration mode by measuring the transmitted signal once it is partially (of  $-30$  dB) diverted toward the calibration port (Cal Port) through the directional coupler, as identified by the dashed green line. The receive calibration mode instead is highlighted in Figure 1b by the green dashed line, since a known reference signal is injected into the receive path by the Cal Port through the directional coupler.

The T/R module housing was manufactured using ISP (integral substrate package) technology. This means that the substrate hosting the T/R module circuits acts as part of

the housing as well. Each housing hosts four T/R modules, this allows for the shrinking of the overall dimensions and thus compliance with the radiating elements pitch required by operations up to 12 GHz. Indeed, grouping the T/R modules allows for the avoidance of double walls and gaps between them. The selected disposition with the connectors toward the radiating element at the module periphery allows for TRM fixation points at the corners (thus assuring a good thermal and mechanical contact of the whole module) and ensures the proper fixation point to the radiating board. In addition, this leads to the simplification of the product structure (allowing for a single cover/frame) and enables future development with multichannel core-chips.

The housing is illustrated in Figure 2.

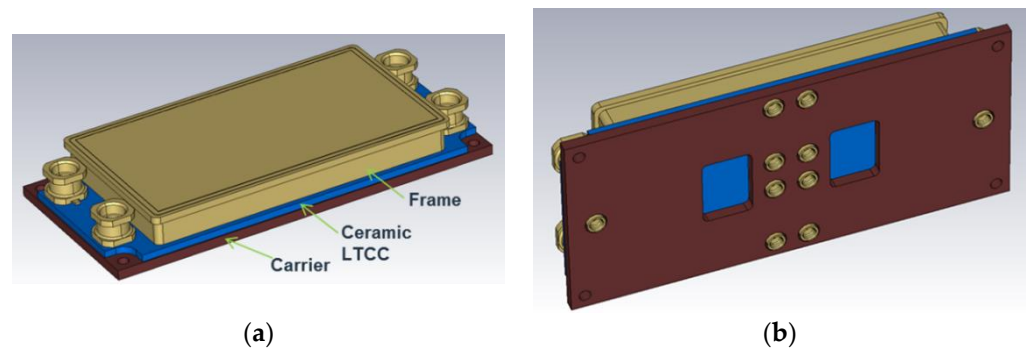


**Figure 2.** Compact packaging solution for hosting the 4 TRMs. (a) Top view. (b) Bottom view.

The complete packaging solution is composed of:

- A molybdenum carrier, which acts as a heat spreader due to its high thermal conductivity;
- A LTCC (low-temperature co-fired ceramics) multilayer substrate [33], which hosts the T/R module circuits;
- A Kovar ring and a Kovar cover, which enclose the top of the substrate.

The LTCC substrate is AuSn soldered on the molybdenum carrier, and the Kovar® ring is also AuSn soldered on the top of the substrate. The Kovar® cover is laser-welded on the Kovar® ring. RF blindmate connectors are directly soldered on the substrate, while DC interconnections are gold pads placed on the bottom of the substrate, which may be accessed through two windows on the molybdenum carrier and contacted using solderless interposers.

The LTCC multilayer substrate, based on a high-frequency, low-dielectric loss tape system manufactured by FERRO (A6M-E), features embedded RF structures inside its inner layers, such as RF transitions, RF couplers, and RF combiners. The design of the RF passive devices and interconnects will be analyzed in detail in Section 3.

### 3. Radio Frequency Design

This section reviews the design of those interconnects and devices of major importance, since they are laid out between the SCFE and the antenna connector. Thus, they should ensure low loss for a minimal degradation of the noise figure (NF) when the TRM works in receiving mode, and to avoid power loss in transmit mode, there should be good impedance matching for avoiding the high power of the transmitted signal bouncing between the SCFE and the antenna, thus degrading the antenna gain.

The TRM portion of interest between the SCFE and the antenna connector is shown in Figure 3. Each single RF line to be accurately designed is enclosed in a yellow rectangle and identified by a specific number from one to four:

- (1) Directional coupler for reaching the calibration port,
- (2) Microstrip (red)–stripline (purple)–microstrip (red) transition from the SCFE output to the coaxial connector toward the antenna,
- (3) Wilkinson power divider in order to have only one Cal Connector for two TRMs,

- (4) Stripline (purple) to coaxial connector transition toward the Cal Port. This transition is similar to the one designed for the TXin and RXout ports at the TRM input, as defined in Figure 1, although the latter involve the transition between the microstrip and the connector on the opposite side of the stack-up.

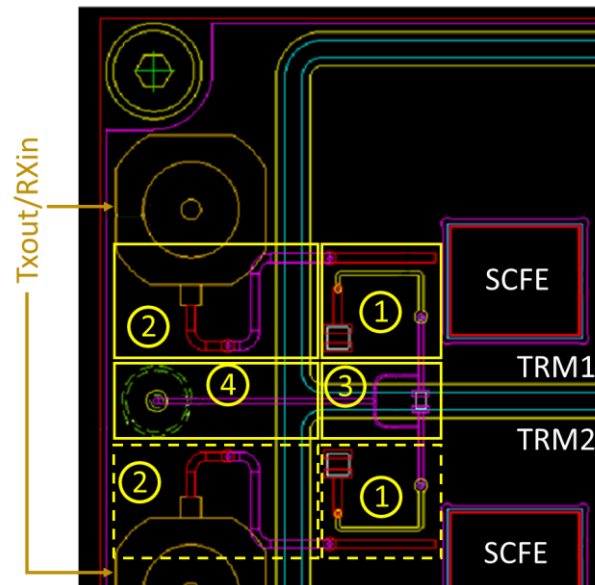


**Figure 3.** Overview of the RF transitions of interest that have been accurately designed.

Since the two TRMs are placed next to each other, the same transitions 1 and 2 belong to both adjacent modules. Such transitions for the TRM2 are enclosed by yellow dashed rectangles.

The design of the RF transition was carried out by combining the advantages of a circuit simulator (Keysight Advanced Circuit Simulator ADS [34]), such as simulation speed and possibility of optimization process based on the simultaneous tuning of multiple geometrical variables, and the accuracy of a full-wave simulation using CST Microwave Studio [35].

### 3.1. Directional Coupler Design

The directional coupler is necessary to couple the SCFE output signal from/to the calibration port. It was designed to have a coupling factor of about  $-30$  dB and a directivity better than 15 dB. The design principle was quite simple, involving a trace close by the SCFE output microstrip, although a fine optimization was necessary to reach the desired values. The initial structure and the port numbering for evaluating the coupler performances are shown in Figure 4. The coupled line is buried in the second stack-up layer to minimize the risk of corona discharge, since the latter is attenuated by the dielectric interposed between the SCFE output microstrip (on the top layer) and the coupled line on the second layer (embedded microstrip type of interconnect). The unneeded port of the directional coupler is loaded by a  $50 \Omega$  termination connected to the ground layer. The  $50 \Omega$  resistor is directly printed on top of the substrate, and on the top layer, there are conductive pads using a conductive material with  $100 \Omega/\square$  resistance. The final design parameters are shown in Figure 5.

### 3.2. RF Transition between the SCFE to the Antenna

The coupler design described in Section 3.1 ends on a microstrip that needs to be connected to the coaxial connector (TXout/RXin in Figure 3) for reaching the antenna. However, the signal cannot be laid out on a microstrip since it needs to go beyond the Kovar rectangular frame, thus being outside the encapsulated TRM. This objective is accomplished by moving the trace toward an inner layer, thus becoming a stripline to

bypass the TRM perimeter, for reaching the top layer again close to the antenna connector. The designed transition is shown in the exploded 3D view in Figure 6. A careful design was carried out by appropriately placing ground vias around the signal vias to ensure a microstrip to stripline transition with a characteristic impedance as close as possible to  $50 \Omega$ . The resulting insertion loss ( $S_{21}$ ) and return loss ( $S_{11}$ ) are shown in Figure 7a,b, respectively.

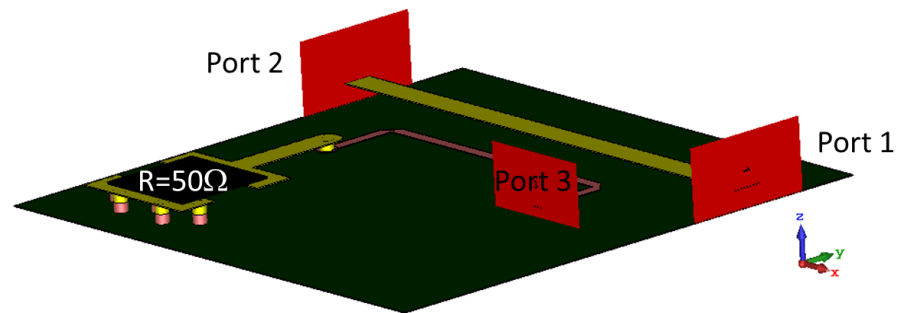


Figure 4. Overview of the directional coupler.

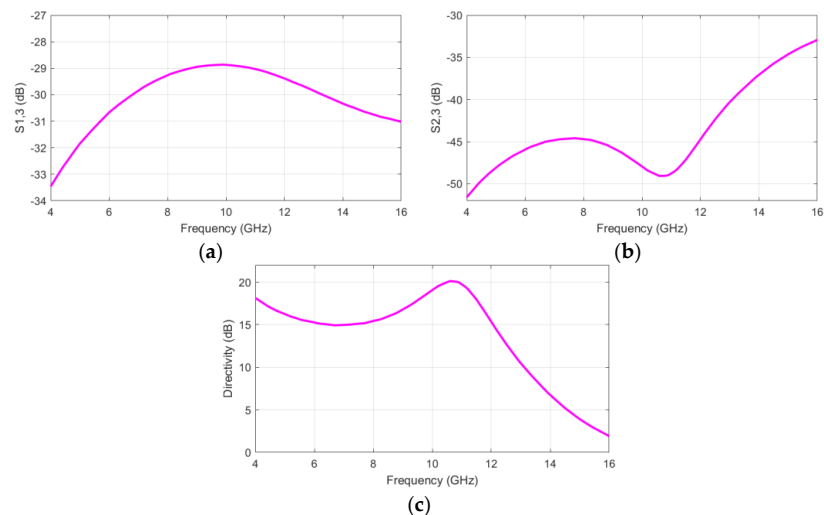


Figure 5. Optimized design of the coupler (final optimized responses highlighted in purple). (a) Coupling factor ( $S_{13}$ ). (b) Isolation ( $S_{23}$ ). (c) Directivity computed as  $D(\text{dB}) = S_{13}(\text{dB}) - S_{23}(\text{dB})$ .

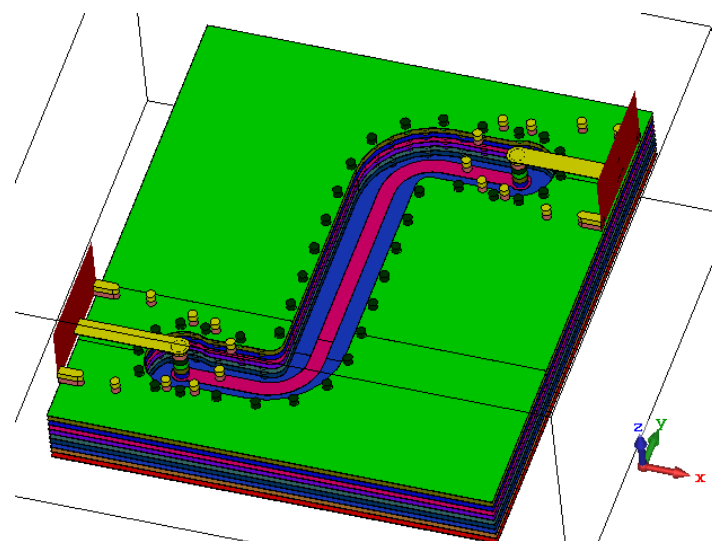
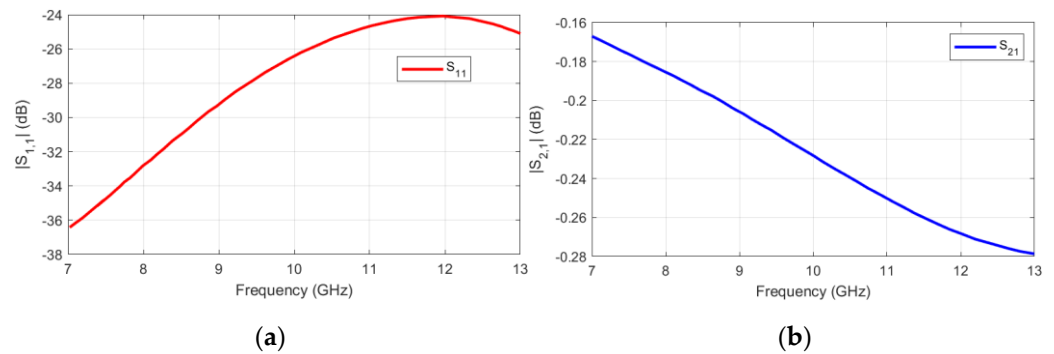


Figure 6. Exploded view of the 3D model used for the transition design.



**Figure 7.** Return loss (a) and insertion loss (b) of the optimized microstrip–stripline–microstrip transition.

### 3.3. Power Divider

A power divider/combine was designed with the objective of reducing the part count, in particular to halve the number of coaxial connectors necessary for TRM calibration. Basically, the proposed solution employs only one calibration connector for two TRMs. The calibration signal during the receive calibration mode is sent to two TRMs; thus, it should be split equally between the TRMs. Additionally, when performing the calibration of the transmitting path of each TRM, the high-power signal at the output of the SCFE is coupled toward the calibration port through the coupler and the Wilkinson divider, with the side TRM being turned off. The power divider was first designed based on well-known theory [36] by selecting the number of stages as two to achieve the required bandwidth. Then, it was implemented into the circuit simulator [35] for refinement and geometry tuning/optimization. Then, the optimized circuit was implemented into the full-wave simulation environment to verify its performances. The equivalent circuit and the full-wave models are reported in Figure 8, whereas the final results in Figure 9 show the comparison of the relevant S-parameters between the circuit and full-wave responses. Specifically, the return loss at Port 1 and at Port 2 (and 3) are shown in Figure 9a,b, whereas the insertion loss and coupling factor are given in Figure 9c,d, respectively. Good agreement was found, although the insertion loss from the full-wave model was affected by the metal and dielectric losses initially neglected in the circuit simulator. Moreover, the slight differences that can be seen in the frequency range 12–14 GHz in Figure 9a,b are mainly due to the coupling between the microstrips, since the circuit model does not take it into account.

### 3.4. RF Transition between Stripline/Microstrip and Coaxial Connector

The design of the RF transitions from the stripline (calibration line) and the microstrip (input TX and out RX) toward the coaxial connectors will be described in this section. The stripline to coaxial transition is shown in Figure 10a, whereas the microstrip to coaxial transition is shown in Figure 10b.

As performed in Section 3.2 for the microstrip–stripline–microstrip transition, the vertical transition was designed to have a characteristic impedance as close as possible to  $50 \Omega$ ; additionally, the diameter of the pads at the signal vias was optimized to avoid an abrupt impedance mismatch at the external layer where a large pad is required for brazing the pin of the coaxial connector.

The optimization of the transition was performed in two steps. The first one involves the vertical transition and a small piece of stripline up to the point where a TEM mode is propagating. A waveguide port [35] was set at the stripline, whereas the output port was defined at the coaxial interface on the substrate external layer; the two-port S-parameter of the transition was obtained through a full-wave simulation. The S-parameter dataset was used within the circuit simulation environment [34], where three transmission line sections were added. Such three sections were optimized for length and width (characteristic impedance) to achieve optimized performances of the  $S_{11}$  and  $S_{21}$ . Once the optimized results were satisfactory, the obtained geometrical parameters (length and width) of the three lines were

translated into actual stripline sections added to the original full-wave model to verify the optimized performances. The final results are reported in Figure 11 for the stripline to coaxial transition, with a comparison between the circuit and full-wave simulation. Good agreement was obtained, thus demonstrating the feasibility of the quick circuit-based optimization compared to the much more time-consuming full-wave optimization.

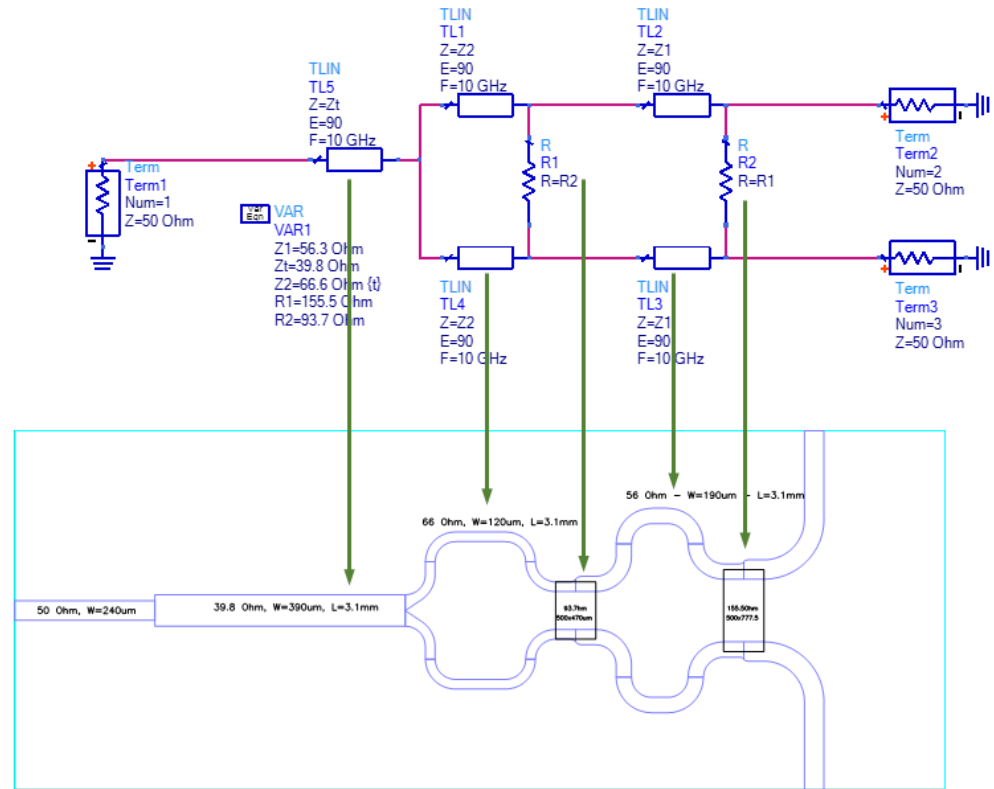


**Figure 8.** Overview of the equivalent circuit model and the corresponding layout within the full-wave simulator.

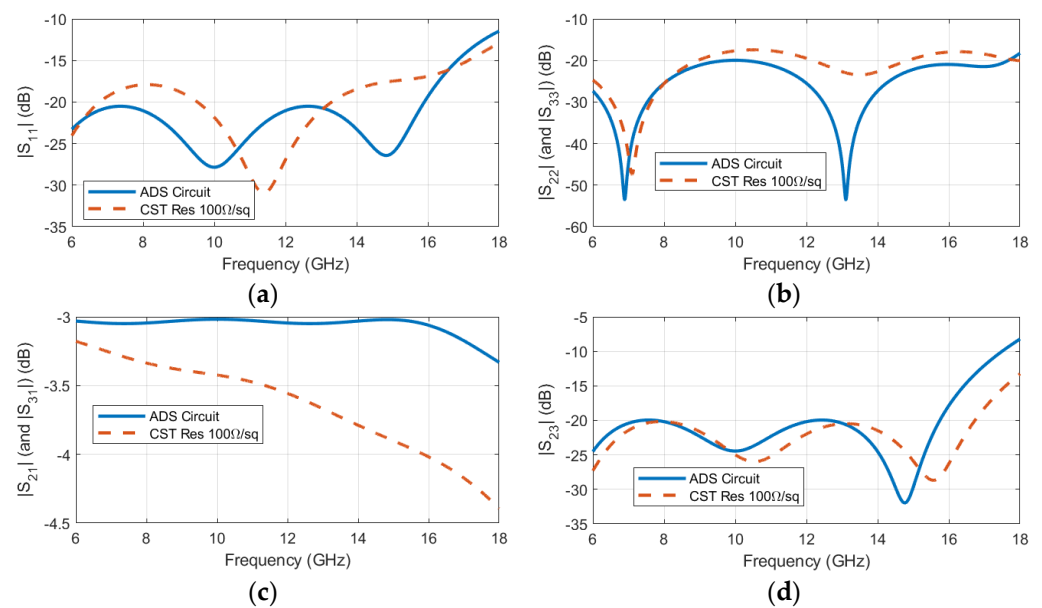


**Figure 9.** S-parameters results and comparison between the circuit and the full-wave model. Specifically, the return loss at Port 1 and at Port 2 (and 3) are shown in (a,b), whereas the insertion loss and coupling factor are given in (c,d), respectively.

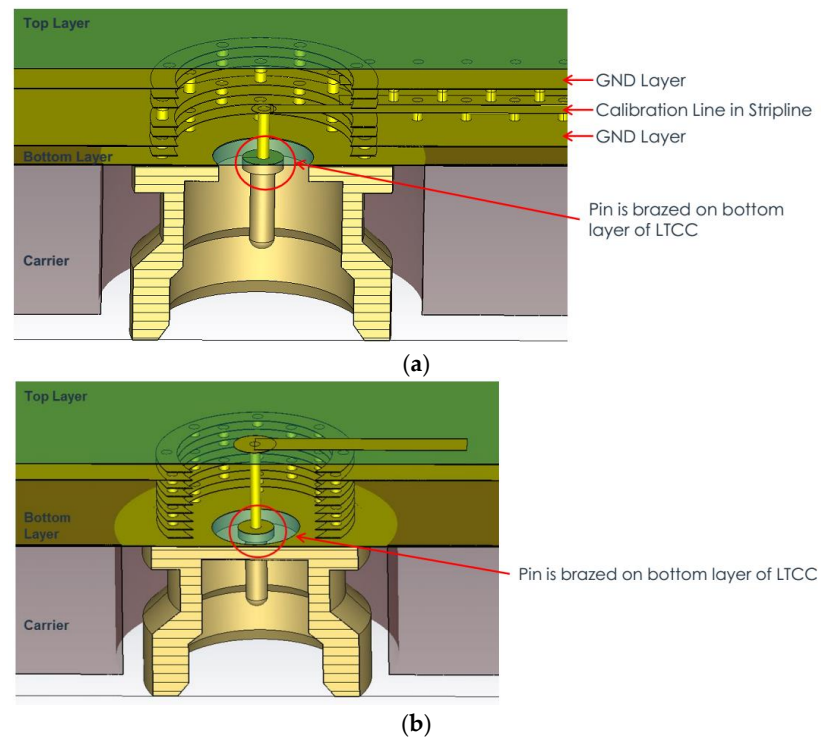


**Figure 10.** Three-dimensional overview of the transitions: (a) stripline to coaxial connector, (b) microstrip to coaxial connector.

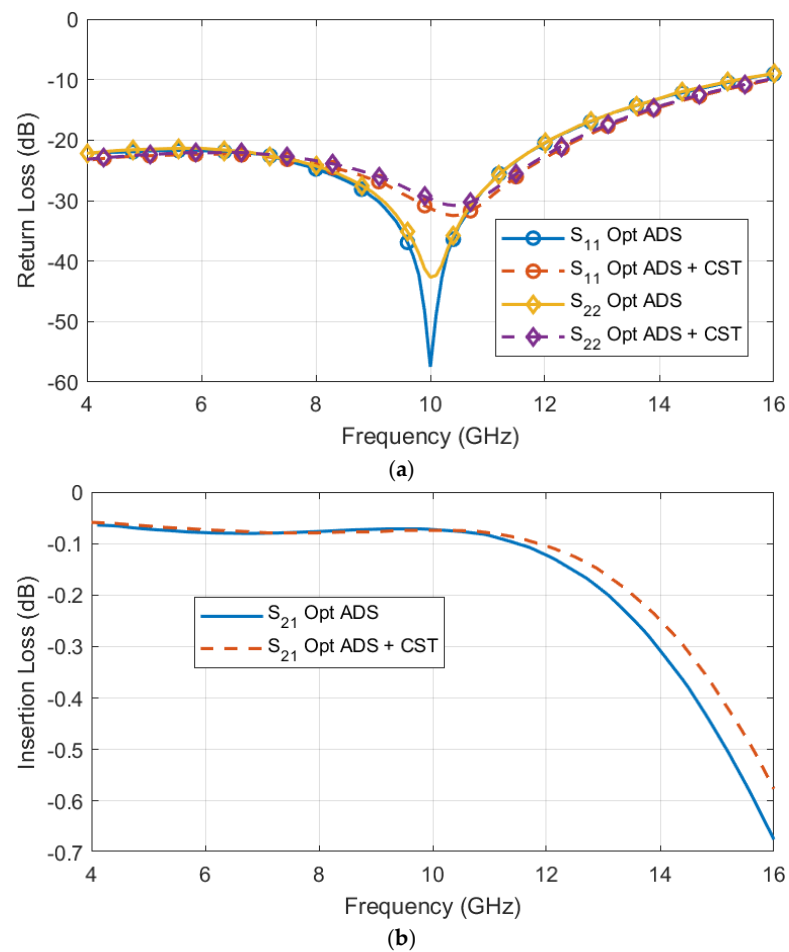
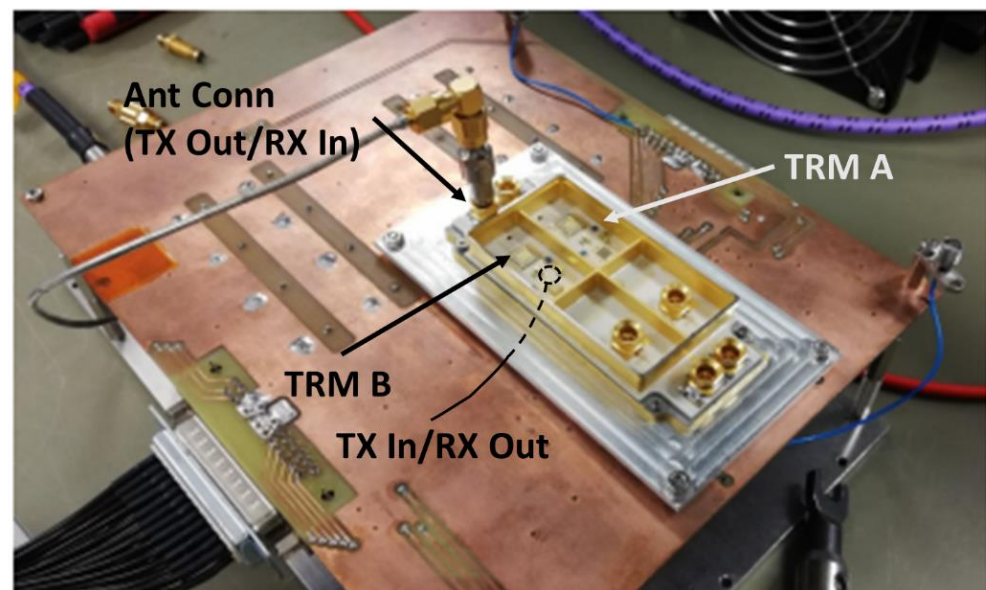


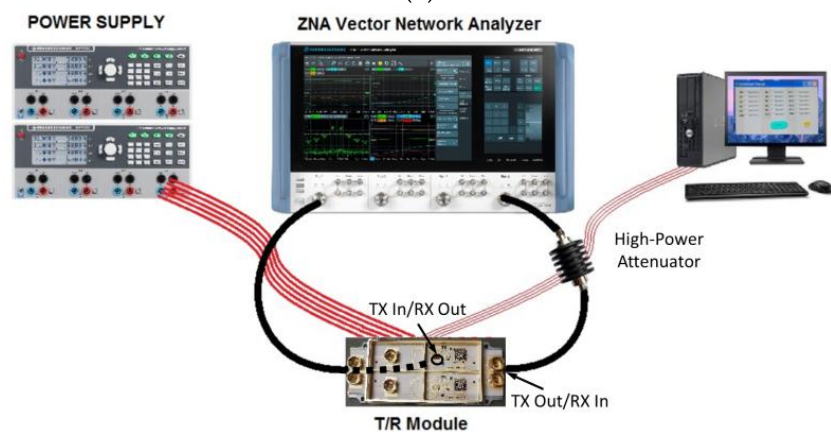
**Figure 11.** Stripline to coaxial connector transition: (a)  $S_{11}$  and  $S_{22}$ , (b)  $S_{21}$ .

#### 4. Experimental Tests

The design of the RF transitions discussed in Section 3 and the complete assembly of the TRM with the SCFE, the core-chip, and the auxiliary amplifiers (LLA and driver) in Figure 1 led to the manufactured TRM shown in the experimental setup in Figure 12 for testing the fully assembled TRM B, whose output (antenna) power was detected by Port 2 of the VNA through the semirigid coaxial cable connected at the TRM antenna connector. The input power was provided to the TRM B by VNA Port 1 through the input coaxial connector placed under the TRM. The output power is a derived value from the input power set at the Port 1 and the gain ( $S_{21}$ ) measured by the VNA. Due to the expensive SCFE and core-chip devices, only two TRMs were fully assembled, whereas the other two were equipped with coaxial connectors for the verification of the passive interconnects.



(a)



(b)

**Figure 12.** (a) Experimental setup of the quad-TRM. (b) Schematic overview of the complete setup.

A PCB card was developed in order to correctly route all the DC and digital control signals to the TRM and generate the pulsed voltage to switch the gates of the power amplifiers of the SCFE. The quad-module TRM was mounted on an aluminum carrier for thermal and mechanical requirements and was screwed to the large PCB. All DC signals, properly RF filtered, were routed on the PCB from the TRM DC pads at the bottom of the module to a multipin connector and, from this, with an appropriate wiring, to the power supply. As for DC signals, all digital signals (i.e., clock, data) were routed, through the

PCB and a dedicated connector, from the digital pads of the TRM to the parallel port of the controller PC.

The relevant experimental data that characterize the TRM in transmit mode are the gain and the transmitted power. They are reported in Figure 13 as the function of the input power for the three frequency values toward the limits and in the middle of the band of interest at 8 GHz and 12 GHz and then 10 GHz, respectively. The gain in Figure 13a is quite constant for input power level below  $-25$  dBm, as expected; then, it decreases while getting close to the maximum power that can be provided by the final HPA stage of the SCFE. In fact, the output power  $P_{out}$  reaches its maximum of 41.5 dBm when the input power  $P_{in}$  exceeds  $-10$  dBm. The transmitting amplification chain is not expected to work in the linear region, but instead in the compressed region to ensure a more constant gain over frequency. Figure 13c shows the gain as the function of frequency evaluated at the 12 dB compression point (c.p.) after setting the input power  $P_{in} = -3$  dBm. The gain variability is within 0.5 dB, thus ensuring the required in-band variation.

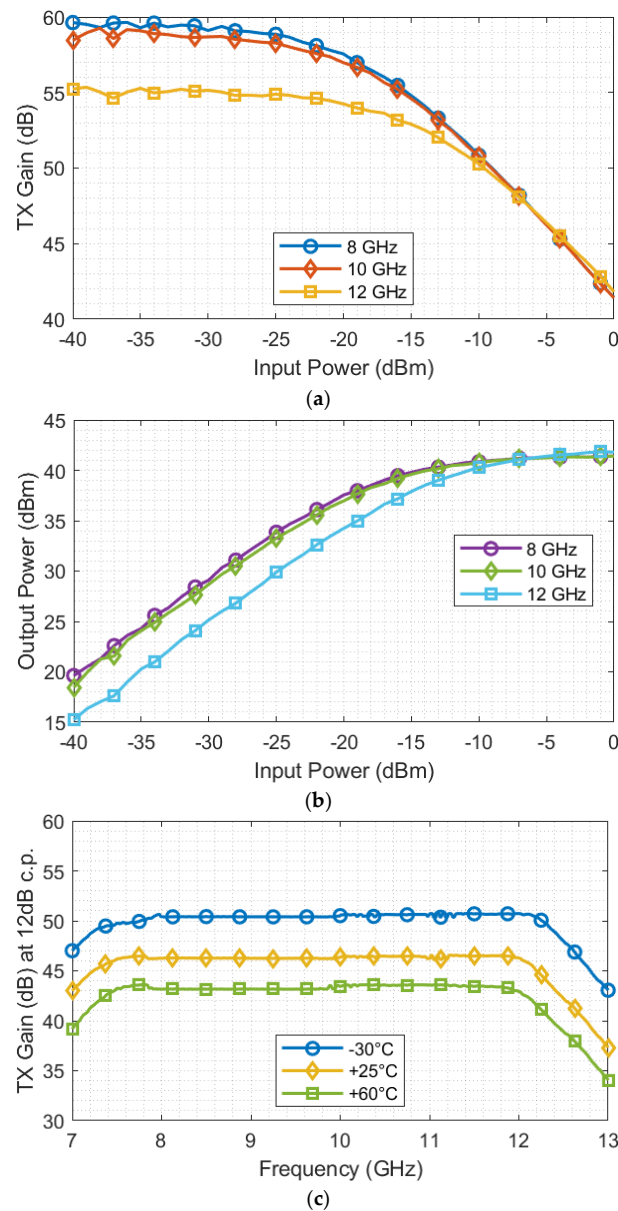
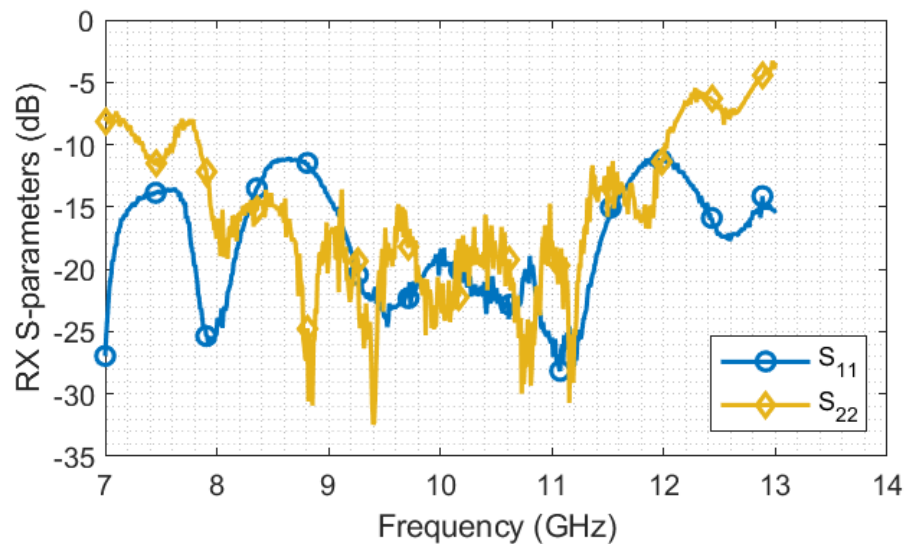


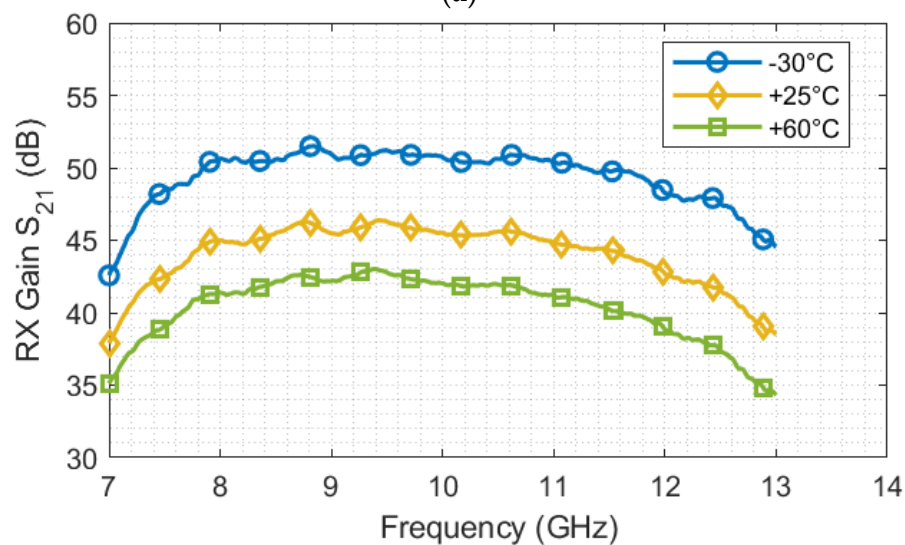
**Figure 13.** (a) TX gain and (b) output power  $P_{out}$  as function of the input power  $P_{in}$ . (c) TX gain at 12 dB compression point ( $P_{in} = -3$  dBm) at three temperatures.

The receive mode is also experimentally characterized by measuring the input and output return loss and the RX gain. The RX chain works in the linear region due to the very low power expected from the antenna. The  $S_{11}$  (from the antenna port) and  $S_{22}$  (from the RXout Port) are shown in Figure 14a, whereas the  $S_{21}$  (RX gain) is reported in Figure 14b. The noise figure (NF) is the last parameter that requires a careful evaluation, since it greatly impacts the sensitivity of the overall RX chain and thus the level of the minimum detectable signal received by the antenna. The procedure for measuring the NF is described by the following steps:

- The Spectrum Analyzer Rohde&Schwarz FSW—Signal and Spectrum Analyzer 2 Hz –50 GHz was set in noise figure mode;
- The noise source HP 346C was connected to the SA to perform the calibration;
- The TRM was placed in the thermal chamber to perform the measurement at a specific temperature;
- The noise source was connected to the antenna connector through a cable with known loss (the loss value was used to de-embed the noise contribution of the cable loss), whereas the RX output connector from the TRM was connected to the SA;
- The NF was measured using the SA.



(a)



(b)

Figure 14. Cont.

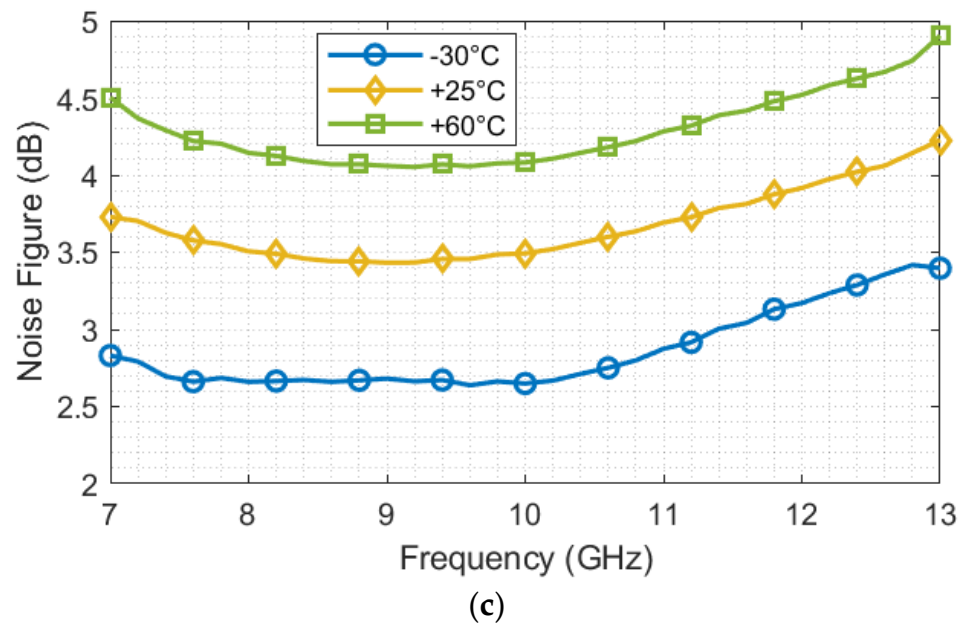


**Figure 14.** (a) Return loss at both ends of the RX chain. (b) Linear RX gain ( $S_{21}$ ) over temperature. (c) Noise figure over temperature.

The NF is within the required limits within the band of interest.

## 5. Conclusions

The design of a complete TRM is discussed in this paper, having extreme performances in terms of transmitted power (41.5 dBm), receiving amplification (up to 46 dB, with the lowest gain of 43 dB at 12 GHz), and a low noise figure (a minimum of 3.4 at low frequency and the highest of 3.9 dB at 12 GHz). The great electrical performances based on a compact and thermally efficient mechanical design demonstrated in this paper will allow for very high-resolution SAR images and large electronically steerable angles. Such performances are ensured in a wide band, thus making this TRM designed and manufactured within a European-funded program a reliable candidate to be included in the development of innovative SAR instruments for the next-generation satellite constellation for Earth observation. One of the main improvements that can be considered for future research is in terms of compactness for even better antenna steering performance, although this poses additional challenges in terms of denser package layout and heat extraction.

**Author Contributions:** Conceptualization, G.M. and A.F. (Antonio Fina), M.A.; methodology, F.d.P., D.D.G. and M.A.; software, F.d.P., A.D.C., P.T. and A.O.; validation, F.d.P., G.M., D.D.G. and M.A.; writing—original draft preparation, F.d.P., A.O.; writing—review and editing, F.d.P., A.D.C., P.T., A.O., G.M., A.F. (Antonio Fina), and M.A.; supervision, G.M. and A.F. (Andrea Fiaschetti); project administration, A.F. (Andrea Fiaschetti). All authors have read and agreed to the published version of the manuscript.

**Funding:** This research is part of the ATOS (Advanced Technological Solutions for X-band Earth Observation Systems) project funded by the European Community under the H2020 Research and Innovation framework program, grant number 776350. <https://cordis.europa.eu/project/id/776350>. (Access date 25 September 2022).

**Informed Consent Statement:** Not applicable.

**Conflicts of Interest:** The authors declare no conflict of interest.

## References

1. Matevosyan, H.; Lluch, I.; Poghosyan, A.; Golkar, A. 'A value-chain analysis for the copernicus earth observation infrastructure evolution: A knowledgebase of users, needs, services, and products. *IEEE Geosci. Remote Sens. Mag.* **2017**, *5*, 19–35. [CrossRef]
2. Alarcón, E.; Sanchez, A.A.; Araguz, C.; Barrot, G.; Bou-Balust, E.; Camps, A.; Cornara, S.; Cote, L.; Peña, A.G.; Lancheros, E.; et al. Design and optimization of a polar satellite mission to complement the copernicus system. *IEEE Access* **2018**, *6*, 34777–34789. [CrossRef]
3. Ma, J.; Sun, W.; Yang, G.; Zhang, D. Hydrological analysis using satellite remote sensing big data and CREST model. *IEEE Access* **2018**, *6*, 9006–9016. [CrossRef]
4. Bian, X.; Shao, Y.; Wang, S.; Tian, W.; Wang, X.; Zhang, C. 'Shallow water depth retrieval from multitemporal sentinel-1 SAR data. *IEEE J. Sel. Topics Appl. Earth Observ. Remote Sens.* **2018**, *11*, 2991–3000. [CrossRef]
5. Joerg, H.; Pardini, M.; Hajsek, I.; Papathanassiou, K.P. Sensitivity of SAR tomography to the phenological cycle of agricultural crops at X-, C-, and L-band. *IEEE J. Sel. Topics Appl. Earth Observ. Remote Sens.* **2018**, *11*, 3014–3029. [CrossRef]
6. Le, B.T.; Xiao, D.; Mao, Y.; He, D.; Zhang, S.; Sun, X.; Liu, X. Coal exploration based on a multilayer extreme learning machine and satellite images. *IEEE Access* **2018**, *6*, 44328–44339. [CrossRef]
7. Boni, G.; Ferraris, L.; Pulvirenti, L.; Squicciarino, G.; Pierdicca, N.; Candela, L.; Pisani, A.R.; Zoffoli, S.; Onori, R.; Proietti, C.; et al. A prototype system for flood monitoring based on flood forecast combined with COSMO-SkyMed and sentinel-1 data. *IEEE J. Sel. Topics Appl. Earth Observ. Remote Sens.* **2016**, *9*, 2794–2805. [CrossRef]
8. Li, S.; Wang, Y.; Chen, P.; Xu, X.; Cheng, C.; Chen, B. Spatiotemporal fuzzy clustering strategy for urban expansion monitoring based on time series of pixel-level optical and SAR images. *IEEE J. Sel. Topics Appl. Earth Observ. Remote Sens.* **2017**, *10*, 1769–1779. [CrossRef]
9. Lazecky, M.; Hlavacova, I.; Bakon, M.; Sousa, J.J.; Perissin, D.; Patricio, G. Bridge displacements monitoring using space-borne X-band SAR interferometry. *IEEE J. Sel. Topics Appl. Earth Observ. Remote Sens.* **2017**, *10*, 205–210. [CrossRef]
10. Chae, S.-H.; Lee, W.-J.; Jung, H.-S.; Zhang, L. Ionospheric correction of L-Band SAR offset measurements for the precise observation of glacier velocity variations on Novaya Zemlya. *IEEE J. Sel. Topics Appl. Earth Observ. Remote Sens.* **2017**, *10*, 3591–3603. [CrossRef]
11. Kim, S.; Song, C.-M.; Lee, S.-H.; Song, S.-C.; Oh, H.-U. Design and Performance of X-Band SAR Payload for 80 kg Class Flat-Panel-Type Microsatellite Based on Active Phased Array Antenna. *Aerospace* **2022**, *9*, 213. [CrossRef]
12. Xu, W.; Deng, Y.; Wang, R. Multichannel synthetic aperture radar systems with a planar antenna for future spaceborne microwave remote sensing. *IEEE Aerosp. Electron. Syst. Mag.* **2012**, *27*, 26–30. [CrossRef]
13. Golkar, A.; Lluch i Cruz, I. The federated satellite systems paradigm: Concept and business case evaluation. *Acta Astron.* **2015**, *111*, 230–248. [CrossRef]
14. Lörcher, M.; Brugger, H. Advanced RF sensors for SAR earth observation using high precision T/R-Modules. In Proceedings of the 2011 3rd International Asia-Pacific Conference on Synthetic Aperture Radar (APSAR), Seoul, Republic of Korea, 26–30 September 2011; pp. 1–6.
15. Di Carlofelice, A.; Tognolatti, P.; Di Giampaolo, E.; Suriani, A. An Ultrawide-band Dual Polarization SAR Antenna for Space Applications. In Proceedings of the 2019 Photonics & Electromagnetics Research Symposium-Spring (PIERS-Spring), Rome, Italy, 17–20 June 2019; pp. 599–603.
16. Andricos, C.; Yueh, S.; Krimskiy, V.A.; Rahmat-Samii, Y. Compact KU-band T/R Module for Wide-Swath High-Resolution Radar Imaging of Cold Land Processes. NASA Tech Briefs Tech. Rep. NPO-46428, Mar. 2010. pp. 27–28. Available online: <https://ntrs.nasa.gov/search.jsp?R=20100009683> (accessed on 20 July 2022).
17. Schuh, P.; Rieger, R.; Fleckenstein, A.; Oppermann, M.; Adelseck, B.; Müssig, H.; Brugger, H. T/R-module technologies today and possible evolutions. In Proceedings of the 2009 International Radar Conference "Surveillance for a Safer World" (RADAR 2009), Bordeaux, France, 12–16 October 2009; pp. 1–5.
18. Mancuso, Y.; Renard, C. New developments and trends for active antennas and TR modules. In Proceedings of the 2014 International Radar Conference, Lille, France, 13–17 October 2014; pp. 1–3.
19. Koliass, N.J.; Borkowski, M.T. The development of T/R modules for radar applications. In Proceedings of the 2012 IEEE/MTT-S International Microwave Symposium Digest, Montreal, QC, Canada, 17–22 June 2012; pp. 1–3.
20. Chippalkatti, V.S.; Biradar, R.C.; Rana, S.S. Technology Trends in Transmit Receive Modules for Synthetic Aperture Radar Satellites. In Proceedings of the IEEE 2022 4th International Conference on Advances in Electronics, Computers and Communications, ICAECC 2022, Bengaluru, India, 10–11 January 2022; ISBN 978-166540239-2.
21. Chen, Z.; Huang, Z.; Zhang, Q.; Zhang, M. Design and research of highly integrated multi-channel tile-type T/R module. *J. Phys. Conf. Ser.* **2021**, *2065*, 012008. [CrossRef]
22. Cho, J.; Jang, D.; Lee, C.-H.; Choo, H. Design of an Interface Layer Using CPW between an Array Antenna and TRM in X-Band Radar Systems to Minimize Leakage Fields and Improve Transmission Characteristics. *Appl. Sci.* **2022**, *12*, 8514. [CrossRef]
23. Tolani, H.; Rao, C.V.N.; Aich, S.; Dhar, J.; Jyoti, R. Hermetically Sealed S-Band LTCC Based Transmit/Receive Module with Integrated Self-Calibration Circuitry for Space-borne SAR. In Proceedings of the 2021 IEEE MTT-S International Microwave Symposium (IMS), Atlanta, GA, USA, 7–25 June 2021; pp. 827–830.
24. Fina, A.; Di Marcantonio, U.; Suriani, A.; Mannocchi, G.; de Paulis, F.; Di Carlofelice, A.; Orlandi, A.; Tognolatti, P. An advanced transmit/receive 3D ceramic hybrid circuit module for space applications. In Proceedings of the 2015 European Microwave Conference (EuMC), Paris, France, 7–10 September 2015; pp. 785–788.

25. Di Carlofelice, A.; de Paulis, F.; Fina, A.; Di Marcantonio, U.; Orlandi, A.; Tognolatti, P. Compact and reliable T/R module prototype for advanced space active electronically steerable antenna in 3-D LTCC technology. *IEEE Trans. Microw. Theory Technol.* **2018**, *66*, 2746–2756. [[CrossRef](#)]
26. Fina, A. Microwave Antenna Module for Space Applications Including a Hybrid Transmit/Receive Module of Package on Package Type. Italian Patent Office, Application Number IT102017000086529; EU Patent 18 186 105.5. U.S. Patent 16/047.407, 27 July 2017.
27. Fina, A.; Di Carlofelice, A.; De Paulis, F. High Power, Thermally Efficient, X-band 3D T/R Module With Calibration Capability for Space Radar. *IEEE Access* **2018**, *6*, 60921–60929. [[CrossRef](#)]
28. Venturini, R.; Spadoni, F.; Croci, R.; Torre, A.; Capece, P.; Caltagirone, F.; Monaci, F. COSMO SG, SAR instrument design. In Proceedings of the EUSAR 2014, 10th European Conference on Synthetic Aperture Radar, Berlin, Germany, 3–5 June 2014; pp. 1–4.
29. Torre, A.; Capece, P. COSMO-SkyMed: The advanced SAR instrument. In Proceedings of the 5th International Conference on Recent Advances in Space Technologies—RAST2011, Istanbul, Turkey, 9–11 June 2011; pp. 865–868.
30. Kaundinya, S.; Karthikeya, G.S. Recent advancements in design of microwave components for space applications. In Proceedings of the 2016 IEEE International Conference on Recent Trends in Electronics, Information & Communication Technology (RTEICT), Bangalore, India, 20–21 May 2016; pp. 206–211.
31. Resca, D.; Scappaviva, F. Design of the power amplifier section of a X-band MMIC single chip front end. In Proceedings of the European Microwave Week (EuMW 2021), Short Course, 13–18 February 2022.
32. Advanced Technological Solutions for X-Band Earth Observation Systems—ATOS Project. Available online: <http://www.atos-h2020.eu/> (accessed on 21 July 2022).
33. Available online: [www.ferro.com](http://www.ferro.com) (accessed on 23 March 2022).
34. Keysight Pathwave Advanced Design Systems ADS. Available online: <https://www.keysight.com/it/en/products/software/pathwave-design-software/pathwave-advanced-design-system.html> (accessed on 27 July 2022).
35. Computer Simulation Technology, CST 2021, Dassault Systeme. Available online: <https://www.3ds.com/> (accessed on 11 February 2022).
36. Pozar, D.M. *Microwave Engineering*, 4th ed.; Wiley: Hoboken, NJ, USA, 2012.

**Disclaimer/Publisher’s Note:** The statements, opinions and data contained in all publications are solely those of the individual author(s) and contributor(s) and not of MDPI and/or the editor(s). MDPI and/or the editor(s) disclaim responsibility for any injury to people or property resulting from any ideas, methods, instructions or products referred to in the content.